Journal of
Materials Chemistry C

ROYAL SOCIETY
OF CHEMISTRY

PAPER

View Article Online
View Journal | View Issue

Check for updates

Cite this: *J. Mater. Chem. C*, 2025, **13**, 8723

Structural phase transition, mechanics, and thermodynamics of heavy fermion metal UPt$_3$ under pressure†

Hao Quan,[abc] Li Li,[a] Jiang-Jiang Ma,[d] Wei-Dong Li[e] and Bao-Tian Wang *[bc]

Received 27th January 2025,
Accepted 19th March 2025

DOI: 10.1039/d5tc00379b

rsc.li/materials-c

Crystal structures, electronic structures, mechanics, and thermodynamics of the heavy fermion superconductor UPt$_3$ under a pressure of up to 300 GPa have been investigated by a particle swarm optimization structure prediction method together with detailed first-principles calculations. A pressure-induced structural phase transition (P_T) is predicted at 155.9 GPa, where the hexagonal crystal structure with the space group $P6_3/mmc$ transforms into an orthorhombic structure with the space group *Cmmm*. The molar volume of UPt$_3$ drops about 2.52% at 155.9 GPa, while the distance between the first-nearest neighbor of U atoms (d_{U-U}) decreases, implying a switch from the heavy electronic states to the weakly correlated electronic states. The metal nature is well retained upon the phase transition and upon further compression to 300 GPa. Phonon dispersions and elastic constants are used to confirm the dynamical and mechanical stability of both phases under different pressures. The bulk modulus B, shear modulus G, and Young's modulus E of the *Cmmm* are all higher than those of the $P6_3/mmc$, indicating enhanced mechanical properties of the *Cmmm* phase at the same pressure. The highest phonon vibration frequency increases with pressure, suggesting strengthened atom–atom interactions. Thermodynamic properties, evaluated using the quasi-harmonic approximation (QHA), reveal that the $P6_3/mmc$ phase remains stable in the 0–155.9 GPa range, while the *Cmmm* phase emerges under higher pressures. Our results provide theoretical insights into the pressure-driven phase transition of UPt$_3$ and provide its detailed electronic, phononic, mechanical, and thermodynamic properties under external pressure.

Introduction

Heavy fermion materials, as typical strongly correlated systems with a high specific heat coefficient, are commonly found in lanthanide or actinide intermetallic compounds containing f electrons.[1–4] Due to the f electrons exhibiting both itinerant and localized states, the unfilled 4f or 5f electron shells coherently hybridize with conduction band electrons to form heavy fermion states. These states give rise to a variety of quantum phenomena, including unconventional superconductivity,[3,5] multiple magnetic order,[6] non-Fermi liquids,[7,8] and topological states.[9] To date, a series of uranium-based heavy fermion superconductors have been extensively studied, such as UTe$_2$,[10] UPt$_3$,[11] and UBe$_{13}$.[12] They exhibit the coexistence of spin-triplet superconductivity and magnetic order.

In UPt$_3$, two distinct superconducting states (A and B phases) were observed at zero field with superconducting transition temperatures (T_c) of around 0.5 K.[13,14] In the B phase, the broken time-reversal symmetry was observed by the polar Kerr effect, providing the evidence of complex, multicomponent nature for its superconducting order parameter.[15,16] After including the effect of magnetic field, UPt$_3$ transitions into a new superconducting state C phase.[17,18] Neutron diffraction experiments have confirmed the coexistence of superconductivity and antiferromagnetic order in both the B and C phases, where the Néel temperature (T_N) is 5 K.[19–21] Notably, all superconducting phases have been identified as topological superconducting states with different topological invariants and surface states.[22] Recently, the angle-resolved photoemission spectroscopy studies have revealed significant quasiparticle renormalization in the electronic structure of UPt$_3$, which can be attributed to the strong

---

[a] *Institute of Theoretical Physics, State Key Laboratory of Quantum Optics and Quantum Optics Devices, Collaborative Innovation Center of Extreme Optics, Shanxi University, Taiyuan, 030006, P. R. China*
[b] *Institute of High Energy Physics, Chinese Academy of Sciences, Beijing, 100049, P. R. China. E-mail: wangbt@ihep.ac.cn*
[c] *Spallation Neutron Source Science Center, Dongguan, 523803, P. R. China*
[d] *School of Physics and Information Engineering, Shanxi Normal University, Taiyuan, 030031, P. R. China*
[e] *Shenzhen Key Laboratory of Ultra Intense Laser and Advanced Material Technology, Center for Intense Laser Application Technology, and College of Engineering Physics, Shenzhen Technology University, Shenzhen, 518118, P. R. China*

† Electronic supplementary information (ESI) available. See DOI: https://doi.org/10.1039/d5tc00379b

correlation effects of the 5f electrons.[23] With its abundant array of quantum phenomena, UPt_3 serves as a paradigmatic system in condensed matter physics, offering a unique platform for exploring heavy-fermion superconductivity and the interplay of competing quantum orders.

Pressure is a crucial parameter to regulate crystal structures, which further influences the electronic and various physical properties of materials. In uranium-based compounds, pressure can induce quantum phase transitions, enhance or suppress superconductivity, modulate magnetic order, and drive other quantum phenomena. For instance, UO_2[24] and UO_3[25] were reported to undergo structural phase transitions under pressure. The volume collapse of UO_3 under high pressure leads to an insulator-to-metal electronic transition.[25] For UGe_2, superconductivity was observed in the pressure range of 1–1.6 GPa, with the highest T_c of approximately 0.7 K at 1.2 GPa.[26–28] A pressure-induced symmetry transition, from *Immm* to *I*4/*mmm*, suggests that less 5f electron participation in bonding due to the weakly correlated superconducting phase appears in the tetragonal structure of UTe_2.[29,30] Spin-triplet *p*-wave superconductivity in UBe_{13} has been revealed through low-temperature high-pressure experiments, providing a direct case of triplet pairing in strongly correlated electron systems.[12] For UPt_3, no structural phase transitions have been observed up to 52 GPa, as confirmed by the X-ray diffraction experiments.[31] However, when the pressure exceeds 0.3 GPa, the low-temperature superconducting A phase was suppressed. Under an external magnet field, the superconducting B phase transformed into the C phase,[32,33] with the C phase being the most stable state under uniaxial pressure.[34] The experimental results of Gouchi *et al.* demonstrated that when the pressure exceeds the critical threshold of 0.4 GPa, the Josephson effect in the B phase was suppressed, leading to significant changes in its superconducting properties.[35] Furthermore, neutron diffraction experiments revealed that pressure not only suppresses the superconductivity but also affects the antiferromagnetic order in UPt_3.[36]

In the present study, we report the discovery of a novel orthorhombic *Cmmm* phase of UPt_3 above 155.9 GPa, obtained through the particle swarm optimization (PSO) structure prediction as well as detailed first-principles calculations. The structure and physical properties of $P6_3/mmc$ and *Cmmm*-UPt_3 are calculated at different pressures. Compared with the $P6_3/mmc$ phase, the volume of the *Cmmm* phase shrinks by about 2.52% and the U–U bond length shortened by 36% at the P_T point. The electronic density of states (DOSs) at the Fermi level, $N(E_F)$, of *Cmmm*-UPt_3 is higher than that of $P6_3/mmc$-UPt_3, and the itinerancy of the U 5f electrons is released upon phase transition. Excellent dynamical and mechanical stabilities of both phases at different pressures are confirmed by calculating the phonon dispersions and elastic constants, respectively. The highest vibration frequency increases with pressure, indicating that the interactions among atoms are strengthened. The elastic moduli *B*, *G*, and *E* of *Cmmm*-UPt_3 are higher than those of $P6_3/mmc$-UPt_3 at P_T. The QHA is used to analyze the thermodynamic properties. Our results clearly illustrate the structural phase transition of an important heavy fermion metal and provide its detailed electronic, phononic, mechanic, and thermodynamic properties under a wide pressure range of 0–300 GPa.

Computational details

The structure predictions in our present work were performed by using the PSO technique as implemented in the CALYPSO code,[37,38] which has been proven to be effective and accurate in predicting the stable and metastable structures of a large variety of materials including actinide compounds.[39–42] An extensive search of stable UPt_3 crystal structures within 1–4 molecular formula units were carried out using CALYPSO between 0 and 300 GPa. As shown in Fig. 1, the candidate eight structures with the lowest enthalpy were picked to optimize with high accuracy to obtain the most stable structure of UPt_3. The structural relaxations and physical properties were determined using the Vienna *ab initio* simulation package (VASP)[43,44] with the projector augmented wave scheme (PAW).[45] The exchange–correlation function with the local density approximation (LDA) was performed to deal with the

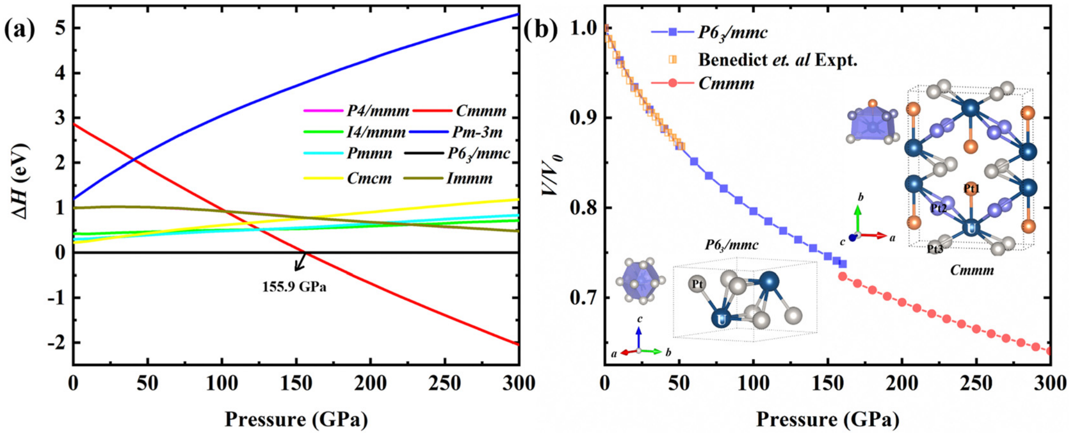

Fig. 1 (a) Relative enthalpy and (b) volume curves as a function of pressure for UPt_3 from 0 to 300 GPa. The enthalpy of the $P6_3/mmc$ phase is set as zero for reference. The experimental results of the $P6_3/mmc$ UPt_3 at 0–50 GPa are presented for comparison.[31]

Kohn–Sham equations.[46] The valence electrons for U and Pt were $6s^26p^66d^25f^27s^2$ and $5d^96s^1$, respectively. The kinetic energy cutoff of 550 eV was set to ensure convergence of total energies and forces better than 1×10^{-6} eV and 0.001 eV Å^{-1}, respectively. The Monkhorst–Pack[47] and Γ-centered *k*-point meshes with a reciprocal space resolution of $2\pi \times 0.03$ Å^{-1} were chosen for the orthorhombic and hexagonal crystals, respectively. Dudarev's type on-site Coulomb repulsion[48] among the localized U 5f electrons was considered. The LDA+*U* scheme has been verified to be effective in better describing the electronic structures and/or magnetic states of UPt_3[49] and other uranium-based compounds.[24,25] Here, the Hubbard effective parameter *U*–*J*, which can be labeled as one single parameter *U* for simplicity, of 2 eV is used.[49] Such value has been carefully checked and selected in our previous study of UPt_3 under ambient conditions.[49]

To characterize the lattice dynamic stability, the density functional perturbation theory (DFPT)[50] as implemented in the PHONOPY code[51] was used to calculate the phonon dispersion curves. The $2 \times 2 \times 2$ supercell and $3 \times 3 \times 4$ ($3 \times 3 \times 2$) *q*-point meshes were utilized in calculations of phonon spectra for different structural phases. At the same time, the QHA[52] was used to reveal the thermal properties and the pressure–temperature (*P*–*T*) diagram.

Results and discussion

1. Pressure-induced phase transition

In this work, a series of pressure points are set to predict the stable phases of UPt_3 in the pressure range of 0 to 300 GPa. After high-precision structural optimization, it is observed that only two phases exhibit the lowest enthalpy within a pressure range of 0–300 GPa: $P6_3/mmc$-UPt_3 and *Cmmm*-UPt_3 [see Fig. 1(a)]. The $P6_3/mmc$-UPt_3 is an experimentally observed phase at ambient pressure[53] and no other competitive structures are discovered during 0–155.9 GPa, which is consistent with the X-ray diffraction results (0–50 GPa) reported by Benedict *et al.*[31] Note that we also check the effects of ferromagnetic and antiferromagnetic states to the relative enthalpy of different phases. As shown in Fig. S1 in the ESI,† the P_T of the nonmagnetic states are close to the results of the ferromagnetic and antiferromagnetic states. In addition, the Néel temperature (T_N) is only 5 K[19–21] for UPt_3. Thus, we only consider the nonmagnetic state in our following discussions. For comparison, Table 1 lists the lattice parameters, Wyckoff positions, energies, and enthalpies for two phases of UPt_3 at different pressures, including data from the previous experiment.[53] For the $P6_3/mmc$ phase, the optimized lattice constant *a*(*c*) is 5.647 (4.932) Å, differing from the experimentally reported values[53] by 1.1 (1.3) % under normal pressure. Fig. S2(a) (ESI†) shows the dependence of the lattice constant on pressure. As pressure increases, the lattice constants of UPt_3 decrease in both phases. When the pressure is up to 155.9 GPa, the *a* and *c* of $P6_3/mmc$-UPt_3 are reduced by 8 and 11%, respectively, corresponding to the a/a_0 and c/c_0 ratio are 0.91 and 0.88. This suggests that the [001] direction of UPt_3 is more sensitive to pressure, demonstrating anisotropic compression behavior. From Table 1, the predicted orthorhombic phase *Cmmm*-UPt_3 (19.806 eV f.u.$^{-1}$) is nearly isenthalpic with the $P6_3/mmc$-UPt_3 (19.805 eV f.u.$^{-1}$) at 155.9 GPa. When $P > 155.9$ GPa, *Cmmm*-UPt_3 is enthalpically more favorable than the $P6_3/mmc$, indicating the phase transition from the $P6_3/mmc$ phase to the *Cmmm* phase at 155.9 GPa. Here, the lattice constants *a*, *b*, and *c* for the high-pressure *Cmmm* phase are 7.691, 10.162, and 2.516 Å, respectively, (see in Table 1). As the pressure increases to 300 GPa, the lattice constants of *Cmmm* phases decrease by 3.6, 3.9, and 4.8% for *a*, *b*, and *c*, respectively. To determine whether the phase transition of UPt_3 is first-order or second-order, the volume–pressure curves for each phase are calculated and are shown in Fig. 1(b). The results show a decreasing behavior in volume upon compression. Notably, a 2.52% volume collapse occurs during the transition from the $P6_3/mmc$ to the *Cmmm* phase at 155.9 GPa, suggesting a first-order. The equation of state (EOS) of UPt_3 are calculated and plotted in Fig. S2(b) (ESI†). For $P6_3/mmc$-UPt_3, the equilibrium volume (V_0) is 136.35 Å^3, and the bulk modulus (*B*) and pressure derivative of *B*(*B*′) are 250.79 GPa and 5.04, respectively. The *B* of $P6_3/mmc$-UPt_3 calculated *via* the EOS is consistent with the *B* value (247.36 GPa) obtained by the Voigt–Reuss–Hill (VRH) method.[54] The V_0, *B*, and *B*′ values of high-pressure phase *Cmmm*-UPt_3 are 135.23 Å^3, 254.54 GPa and 5.06, respectively. Meanwhile, the spin–orbital coupling (SOC) effect is considered to reveal the P_T pressure of UPt_3. As shown in Fig. S3 (ESI†), the P_T pressure is approximately 179 GPa with SOC, when $P6_3/mmc$-UPt_3 transformed into *Cmmm*-UPt_3. Due to the P_T pressure without the SOC effect is lower than that with the SOC effect and there are no experimental results to verify, and also since

Table 1 Calculated lattice parameters (Å, deg), Wyckoff positions, energy (eV f.u.$^{-1}$), and enthalpy (eV f.u.$^{-1}$) of UPt_3 phases at select pressures (GPa)

Space group	Pressure	Lattice parameters	Wyckoff positions	Energy	Enthalpy
$P6_3/mmc$	0	$a = b = 5.647$, $c = 4.932$ $\alpha = \beta = 90°$, $\gamma = 120°$ $a = b = 5.712$, $c = 4.867$[53]	U 2c 0.333 0.667 0.250 Pt 6h 0.833 1.667 0.250	−35.75	
	155.9	$a = b = 5.168$, $c = 4.363$ $\alpha = \beta = 90°$, $\gamma = 120°$		−29.29	19.806
Cmmm	155.9	$a = 7.691$, $b = 10.162$, $c = 2.516$ $\alpha = \beta = \gamma = 90°$	U 4j −0.5 −0.115 0.5 Pt1 4j −0.5 0.365 0.5 Pt2 4e −0.25 0.25 0.0 Pt3 4g −0.224 0.0 0.0	−28.03	19.805
	300	$a = 7.412$, $b = 9.760$, $c = 2.395$		−19.93	

the inclusion of SOC is very expansive in calculations, SOC is not considered in the subsequent calculations.

Different from $P6_3/mmc$-UPt$_3$, the Wyckoff positions of U and Pt in $Cmmm$-UPt$_3$ are: U 4j (−0.5, −0.115, 0.5), Pt 4j (−0.5, 0.365, 0.5), 4e (−0.25, 0.25, 0.0), and 4g (−0.224, 0.0, 0.0). As illustrated in Fig. 1(b), a 9-coordinated "single-capped cube" is featured in the high-pressure $Cmmm$ phase and it originated from the 12-coordinated U–Pt tetra-decahedron in the $P6_3/mmc$ phase. From Fig. S4 (ESI†), it can be found that the three bond angles between Pt–U–Pt are 60.80°, 59.20°, and 60.33° in $P6_3/mmc$. The minimum and maximum bond angles in the $Cmmm$ phase are 54.89° and 101.97°, respectively. In the $Cmmm$ phase, the nearest neighbor U–Pt1 distance is 2.538 Å, which is slightly shorter than the U–Pt distance (2.653 Å) in the $P6_3/mmc$ UPt$_3$ phase. The other U–Pt2 and U–Pt3 distances in the $Cmmm$ phase are 2.675 and 2.729 Å, respectively. For U compounds, the Hill limit (∼3.5 Å) represents the boundary between localization and delocalization of the 5f electrons.[55] In observing the behavior of $P6_3/mmc$-UPt$_3$ under pressure (0–155.9 GPa), the U–U bond length ($d_{\text{U–U}}$) decreases from 4.090 Å[49] to 3.696 Å, indicating that the 5f electrons become more itinerant under pressure. The $d_{\text{U–U}}$ in the $Cmmm$ is 2.349 Å, significantly shorter than that in the $P6_3/mmc$ (3.696 Å) at 155.9 GPa, indicating a stronger interaction between U atoms in $Cmmm$-UPt$_3$. This high-to-low symmetry structural transition suggests more 5f electron participation in transferring.[30]

2. Electronic structure

As is well known, crystal structural transition often leads to electron redistribution, which underlines the importance of studying the pressure-induced electronic transition in materials. To obtain further insight into the electronic properties of UPt$_3$

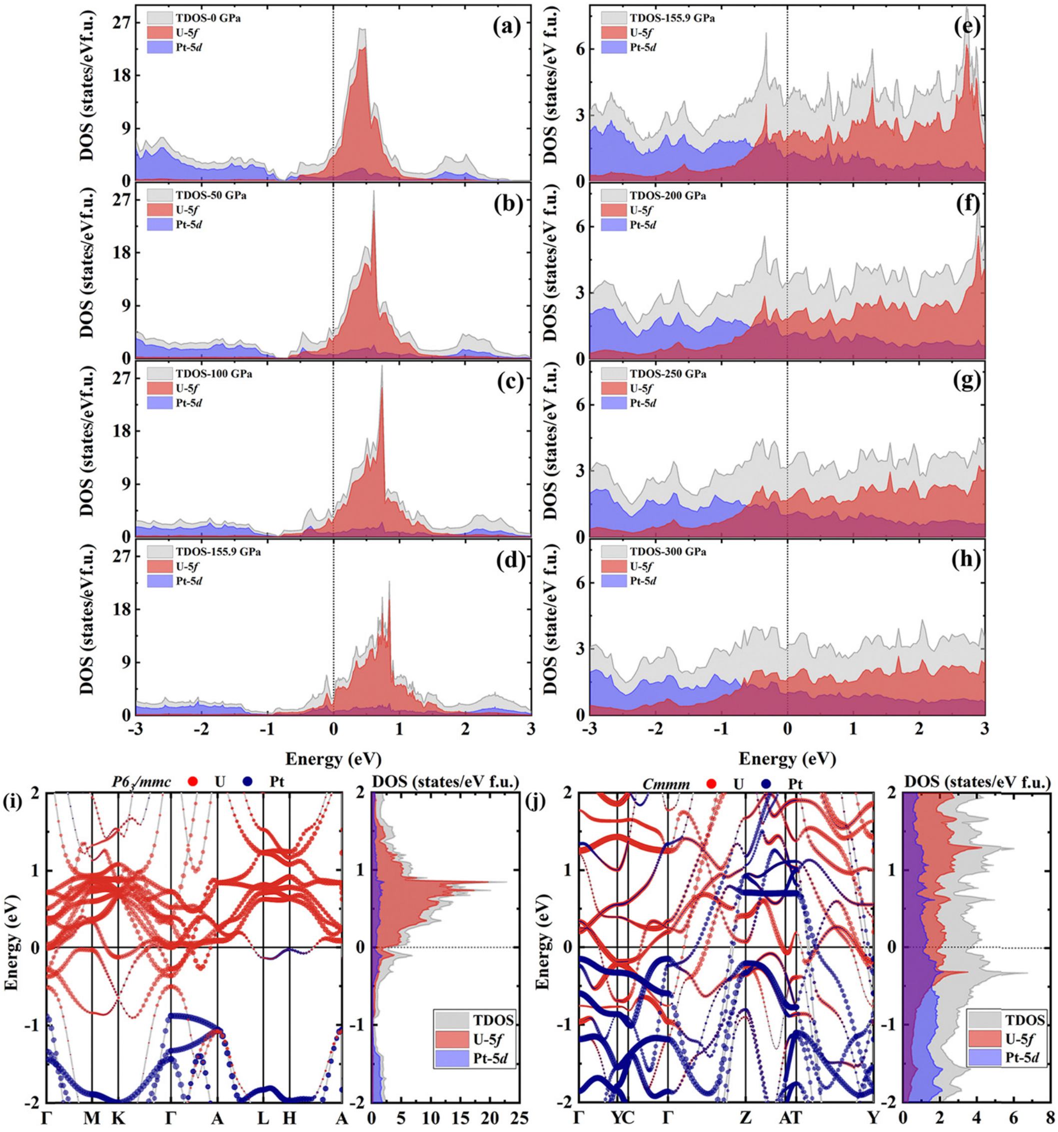

Fig. 2 TDOSs and PDOSs for (a)–(d) $P6_3/mmc$ and (e)–(h) $Cmmm$-UPt$_3$ at different pressures. (i) and (j) Electronic band structures, TDOSs, and PDOSs for UPt$_3$ at 155.9 GPa.

under different pressures, we calculate the total electronic density of states (TDOSs) as well as the projected density of states (PDOSs) of the $P6_3/mmc$- and $Cmmm$-UPt$_3$, as shown in Fig. 2. In $P6_3/mmc$, the Van Hove peaks associated with U-5f orbitals, located between −0.5 and 1 eV at 0 GPa, transform into broader energy levels (−1 to 2 eV) at 155.9 GPa. Meanwhile, in the $Cmmm$ phase, the U-5f DOS peaks at −0.3 eV gradually disappear as the pressure increases from 155.9 GPa to 300 GPa. As seen in Fig. 3(a), the DOSs at the Fermi level, $N(E_F)$, decrease as pressure increases both in the $P6_3/mmc$ and $Cmmm$ phases. The $N(E_F)$ of the $P6_3/mmc$ phase decreases from 5.78 to 3.22 states per eV f.u. as the pressure increases from 0 to 155.9 GPa. In the $Cmmm$ phase, the $N(E_F)$ further declines from 3.84 states per eV f.u. at 155.9 GPa to 3.08 states per eV f.u. at 300 GPa. The $N(E_F)$ in the $P6_3/mmc$ phase is lower than that in the $Cmmm$ phase at 155.9 GPa, indicating that the metallicity of $P6_3/mmc$-UPt$_3$ is weaker than that of $Cmmm$-UPt$_3$. For both $P6_3/mmc$- and $Cmmm$-UPt$_3$, the contribution of Pt-5d orbitals to the Fermi level is slightly lower than that of U-5f orbitals. Although pressure diminishes the metallic characteristics of UPt$_3$, it does not induce a insulator-to-metal transition like that observed in UO$_3$.[25]

It can be seen from Fig. 2 that the U-5f electrons occupy the conduction and several valence bands (−1 to 0 eV), while the lower valence band energy levels are localized mainly by the Pt-5d electrons. In the $Cmmm$ phase, the contribution of both U-5f and Pt-5d states to the valence and conduction bands near the Fermi level suggests hybridization between U-5f and Pt-5d electrons. Compared to the localized 5f electrons in the $P6_3/mmc$ phase, the 5f electrons in the $Cmmm$ phase exhibit more itinerant behavior. Pressure and the structural transition suppress the localization of U-5f electrons, which may be associated with the reduction in the U–U distance.

The Bader charges of U and Pt atoms under different pressures are calculated and are presented in Fig. 3(b). The average valence state of U (Pt) for $P6_3/mmc$-UPt$_3$ decreased from +1.682 (−0.560) at 0 GPa to +1.414 (−0.471) at 155.9 GPa, while for the $Cmmm$ phase, the U atom loses electrons, decreasing from 0.812 to 0.701 *e* over the pressure range of 155.9–300 GPa. The calculated partial charges of UPt$_3$ at 155.9 GPa are listed in Table 2. In the $P6_3/mmc$ and $Cmmm$ phases, each U atom loses 1.414 and 0.812 electrons, respectively, with these electrons being unevenly distributed around the Pt atoms, indicating an anisotropic bonding environment. Similar to U$_2$X (X = Nb and Zr)[39,56] and U–Te systems,[30,57] the differences in charge transfer of U atoms between the two phases indicate that the structural phase transition leads to a redistribution of the electrons. The electron localization function (ELF) is generally used to characterize the localized distribution of electrons. The ELF values are defined as 0, 0.5, and close to 1, corresponding to non-localized electrons, electron gas, and strong electrons, respectively.[58] In both the $P6_3/mmc$ and $Cmmm$ phases, the high ELF regions are 0.819 and 0.833 at 155.9 GPa, respectively, and are mainly concentrated around U atoms, as shown in Fig. S5 (ESI†). For $P6_3/mmc$-UPt$_3$, the localized electrons around the U atom form a "hexagonal ring". Meanwhile, both U and Pt ions are immersed in an almost uniform electron sea with a normalized electron density around 0.4, indicating a typical metallic bond combination.

3. Mechanical properties

In addition to the electronic properties, pressure-induced structural phase transitions can also induce changes in mechanical properties, including elasticity, Debye temperature, Hardness, *etc.*[24,25] The elastic constants C_{ij} of the material are essential for understanding its mechanical stability, ductility, plasticity, and anisotropy. The C_{ij}, elastic moduli (B, G, and E), sound velocities (v_t, v_l, and v_m), and Debye temperature (θ_D) for the two phases of UPt$_3$ are calculated at different pressures, as summarized in Fig. 4. Obviously, all the elastic constants of UPt$_3$ at different pressures are positive and also satisfy the corresponding stability criteria[59] of the hexagonal and orthorhombic crystals. Thus, both the $P6_3/mmc$ and $Cmmm$ phases are mechanically stable at corresponding pressures. Based on the modified criterion,[60] UPt$_3$ is mechanically unstable at 90 GPa, as indicated by the negative value $C'_{44} = C_{44} - P < 0$ (Fig. S6, ESI†). For high-pressure mechanically unstable materials α-quartz and AlO, the phonon spectrum exhibits negative frequencies, and the modified criteria are not satisfied.[61,62] However, UPt$_3$ is dynamically

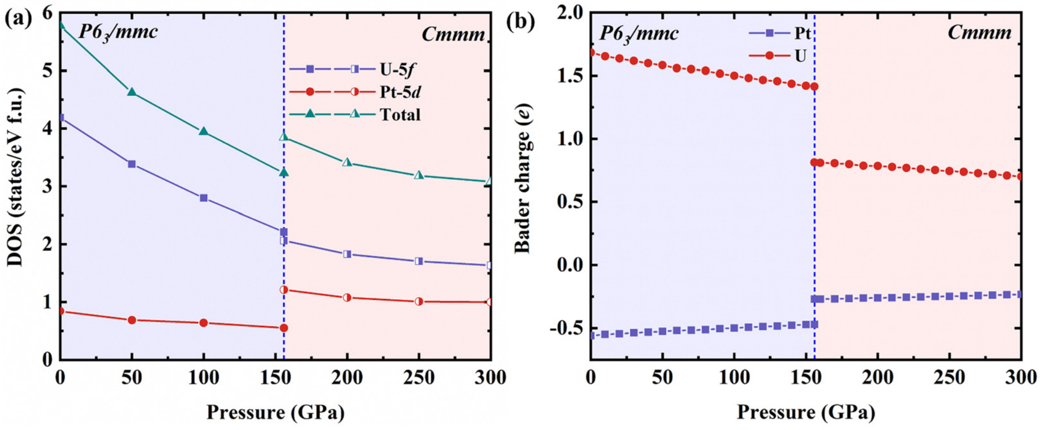

Fig. 3 (a) Total $N(E_F)$ as well as $N(E_F)$ of the U-5f and Pt-5d orbitals and (b) averaged Bader charges of U and Pt atoms in each UPt$_3$ phase.

Table 2 Compared bond length (Å), band angles (deg °) and partial charges (eV atom^{-1}) for U and Pt of UPt_3 at 155.9 GPa

Space group	Bond	Bond length	Bond angels		Atom	Partial charge
$P6_3/mmc$	U–U	3.696			U	+1.414
	U–Pt1	2.653	Pt1–U–Pt2	60.33	Pt1	0.483
	U–Pt2	2.584	Pt2–U–Pt2	60.80/59.20	Pt2	0.449
$Cmmm$	U–U	2.341	Pt1–U–Pt2	59.19	U	+0.812
	U–Pt1	2.538	Pt2–U–Pt3	56.24	Pt1	−0.168
	U–Pt2	2.675	Pt2–U–Pt2	56.10/91.89	Pt2	−0.329
	U–Pt3	2.729	Pt3–U–Pt3	54.89/101.97	Pt3	−0.314

stable within the pressure range shown in Fig. 5 and Fig. S7 (ESI†), indicating that UPt_3 is metastable. Of course, the mechanical stability of UPt_3 under high pressure requires further theoretical and experimental works to verify. For $P6_3/mmc$, the C_{ij} $(i, j \neq 4, 6)$ exhibits an obviously increasing trend with pressure. The slopes of C_{44} and C_{66} related to shear deformation with increasing pressure are smaller than other C_{ij} $(i, j \neq 4, 6)$. In addition, the changes of B, G, and E with pressure are consistent with our previous study of Mott–Hubbard insulator UO_2[24] and metal Zr.[63] It is worth noting that, within the pressure range of 120–155.9 GPa, the C_{33} and C_{44} values of the $P6_3/mmc$ phase exhibit slight oscillations. This phenomenon may suggest that UPt_3 could be in the transition stage of transforming into a new phase. As shown in Fig. S8 (ESI†), similar trends to those of C_{44} can be observed in the pressure-dependence of G, E, ν_t, ν_l, ν_m, and θ_D as well. These behaviors can be attributed to the interdependence [eqn (S1)–(S5) in ESI†] between C_{44} and these parameters. The detailed elastic constants C_{ij} of UPt_3 at 155.9 GPa are presented in Table 3. The values of C_{22} and C_{33} for the $Cmmm$ phase are 1165.1 and 1020.6 GPa, respectively, which are higher than those of the $P6_3/mmc$ phase. This indicates that the b and c directions of the $Cmmm$ phase exhibit greater resistance to compression at 155.9 GPa. However, the resistance along the a direction of the $Cmmm$ is slightly weaker than that of the $P6_3/mmc$ phase, as the C_{11} value for the former is lower than that of the latter. Meanwhile, the C_{ii} $(i = 1–3)$ is higher than the C_{jj} $(j = 4–6)$, indicating greater resistance to the axial compression than shear deformation in both $P6_3/mmc$ and $Cmmm$ phases of UPt_3.

The B, G, and E are evaluated by the VRH approximations.[54] From Table 4, the polycrystalline moduli B, G, and E of the

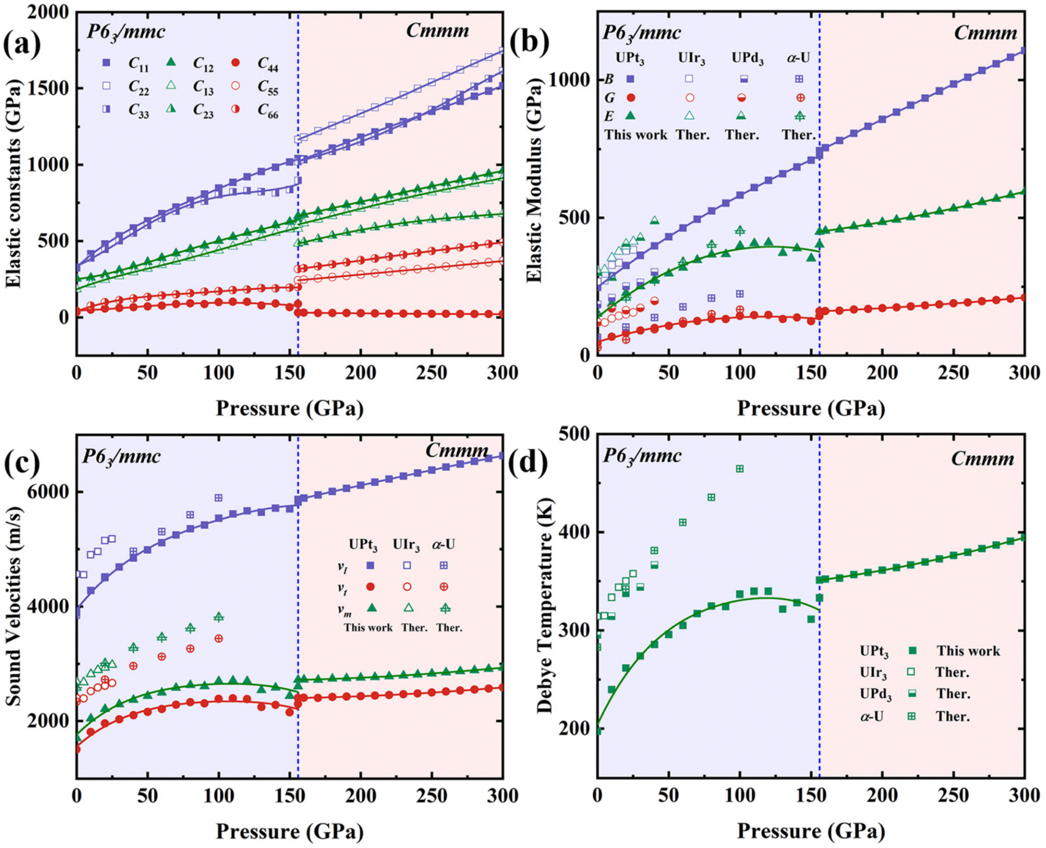

Fig. 4 Calculated (a) elastic constants, (b) elastic moduli, (c) sound velocities, and (d) Debye temperatures as a function of pressure for UPt_3. While the points stand for the calculated values, the solid curves are derived from the polynomial fitting of the calculation data. For comparison, the theoretical data of α-U,[64] UIr_3,[65] and UPd_3[66] are provided.

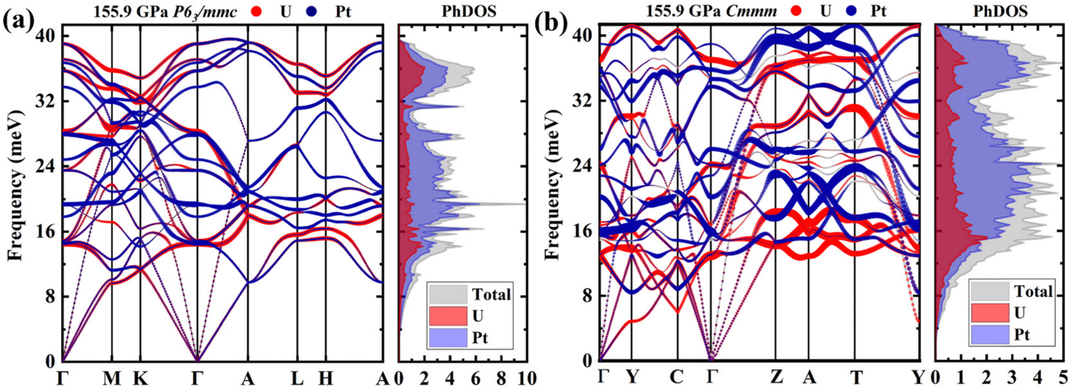

Fig. 5 Calculated phonon dispersions as well as PhDOSs for (a) $P6_3/mmc$-UPt$_3$ and (b) $Cmmm$-UPt$_3$ at 155.9 GPa.

Table 3 Calculated elastic constants C_{ij} (in GPa) of UPt$_3$ at 155.9 GPa

Space group	C_{11}	C_{12}	C_{13}	C_{22}	C_{23}	C_{33}	C_{44}	C_{55}	C_{66}
$P6_3/mmc$	1040.5	640.2	580.6			897.4	88.5		200.2
$Cmmm$	1022.7	663.6	608.1	1165.1	482.6	1020.6	31.9	244.4	318.2

Cmmm phase are larger than those of the $P6_3/mmc$ phase, indicating that the mechanical properties of the high-pressure *Cmmm* phase are superior at 155.9 GPa. For comparison, we provide the result of B, G, and E for α-U,[64] UIr$_3$,[65] and UPd$_3$[66] at different pressures in Fig. 4(b). As shown, the pressure-induced behaviors for these mechanical properties for these compounds are similar. With respect to α-U,[64] which shows brittle elasticity at ambient pressure as reflected by the low values of B/G, alloying with Pt, Ir, and Pd greatly enhances the bulk modulus B and change the brittle nature to ductile. Alloying with platinum, the shear modulus G and Young's modulus E are enhanced slightly with respect to α-U.[64] Compressing over around 40 GPa, the G and E for UPt$_3$ become lower than those of orthorhombic α-U.[64] The B/G and σ values for the $P6_3/mmc$ (*Cmmm*) phase of UPt$_3$ at 155.9 GPa are 5.09 (4.63) and 0.41 (0.40), respectively, both exceeding the thresholds of the Pugh's criteria (1.75) and Poisson's ratio (0.26), respectively. The B/G and σ of UPt$_3$ are close to those of gold (5.39 and 0.45),[67] indicating that UPt$_3$ has the similar elasticity to that of pure gold. These results provide direct evidence that UPt$_3$ exhibits ductile properties in both the $P6_3/mmc$ and *Cmmm* phases at 155.9 GPa. According to the results shown in Table 4, we conclude that both $P6_3/mmc$ and *Cmmm*-UPt$_3$ exhibit strong anisotropy ($A^U > 0$), with the latter showing more pronounced anisotropy due to its lower structural symmetry.

At the same time, the sound velocities (ν_t, ν_l, and ν_m) and Debye temperature θ_D are calculated using the elastic constants. As pressure increases, the ν_t, ν_l, ν_m and θ_D of UPt$_3$ increase steadily. The growth rates of ν_t, ν_l, ν_m and θ_D in the $P6_3/mmc$ phase initially decrease and then fluctuate between 120 and 155.9 GPa, while ν_t, ν_l, ν_m and θ_D increase almost monotonically during the pressure range of 155.9–300 GPa for the *Cmmm* phase. The variations of these parameters clearly indicate that pressure enhance atomic interactions and strengthens atomic bonding. The obtained values of ν_t, ν_l, ν_m, and θ_D for the $P6_3/mmc$ and *Cmmm* phases at 155.9 GPa are presented in Table 4. The θ_D of the *Cmmm* phase is higher than that of the $P6_3/mmc$ phase, indicating that the phase transition from $P6_3/mmc$ to *Cmmm* enhances the bonding ability of UPt$_3$. As shown in Fig. 4, the ν_m and θ_D of UPt$_3$ in pressure range of 0–25 GPa are largely lower than those of UIr$_3$[65] and UPd$_3$,[66] which can be attributed to the heavier atomic mass of Pt compared to Ir and Pd and also can be reflected by low values of G for UPt$_3$.

4. Dynamic and thermodynamic properties

Here, the phonon vibrational properties of UPt$_3$ under different pressures are calculated to evaluate its dynamical stability. As shown in Fig. S7 (ESI†) and Fig. 5, the phonon spectra for both the $P6_3/mmc$ and *Cmmm* phases of UPt$_3$ exhibit dynamic stability at all pressures, confirming their dynamical stability. The coupling between the optical and acoustic modes in the $P6_3/mmc$ and *Cmmm* phases is clearly observable. With increasing pressure, the highest frequency of the optical branch increases from 22 meV to 39 meV in the $P6_3/mmc$ phase (0–155.9 GPa) and from 42 meV to 53 meV in the *Cmmm* phases (155.9–300 GPa). These results clearly indicate that pressure can strengthen the interaction between cations and anions in UPt$_3$. By comparing the phonon dispersions of the $P6_3/mmc$ and *Cmmm* phases at 155.9 GPa (Fig. 5), it is observed that the

Table 4 Calculated elastic moduli (B, G, and E, in GPa), B/G ratio, Poisson's ratio (σ), transverse ν_t (m s^{-1}), longitudinal ν_l (m s^{-1}), average ν_m (m s^{-1}) sound velocities, and Debye temperature θ_D (K) of UPt$_3$ at 155.9 GPa

Space group	B	G	E	B/G	A^U	σ	ν_l	ν_t	ν_m	θ_D
$P6_3/mmc$	727.3	143.0	402.0	5.09	0.84	0.41	5820.82	2297.57	2603.64	333.0
$Cmmm$	743.7	160.5	449.3	4.63	5.26	0.40	5869.28	2402.92	2719.90	350.9

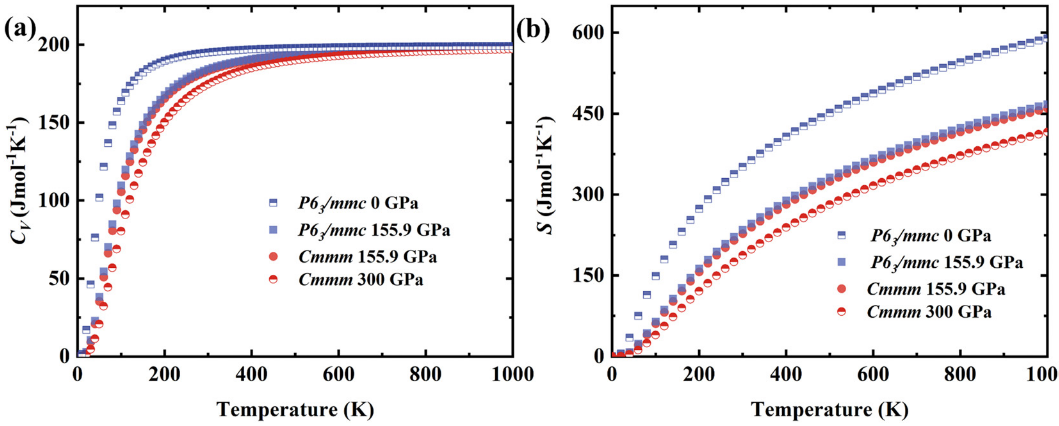

Fig. 6 Temperature dependencies of (a) specific heat at constant volume and (b) entropy of UPt_3.

highest vibration frequency of the *Cmmm* phase is higher than that of the $P6_3/mmc$ phase, indicating stronger bonding and greater lattice stiffness of the former one, which may contribute to its superior mechanical properties. Similar to the phononic results at ambient pressure,[49] both the U and Pt atomic vibrations contribute widely in the full energy range for both $P6_3/mmc$ and *Cmmm* phases. The rigid dispersions of the acoustic branches clearly demonstrate their excellent mechanical properties. The flat phonon bands as well as the van Hove singularities of the bands contribute evident peaks in the phonon density of states (PhDOSs).

According to the group theory analysis of the $P6_3/mmc$ and *Cmmm* space groups, the symmetry decomposition of the modes are as follows.

For $P6_3/mmc$, $\Gamma_{\text{acoustic}} = \mathrm{A}_{2u} \oplus \mathrm{E}_{1u}$,

$$\Gamma_{\text{optical}} = \mathrm{A}_{1g} \oplus \mathrm{A}_{2g} \oplus \mathrm{A}_{2u} \oplus \mathrm{B}_{1u} \oplus \mathrm{B}_{2u} \oplus 2\mathrm{B}_{2g} \oplus 2\mathrm{E}_{1g} \oplus 6\mathrm{E}_{2g} \oplus 4\mathrm{E}_{1u} \oplus 2\mathrm{E}_{2u}.$$

For *Cmmm*, $\Gamma_{\text{acoustic}} = \mathrm{B}_{1u} \oplus \mathrm{B}_{2u} \oplus \mathrm{B}_{3u}$,

$$\Gamma_{\text{optical}} = 3\mathrm{B}_{1u} \oplus 4\mathrm{B}_{2u} \oplus 4\mathrm{B}_{3u} \oplus 3\mathrm{B}_{1g} \oplus \mathrm{B}_{2g} \oplus 2\mathrm{B}_{3g} \oplus \mathrm{A}_u \oplus 3\mathrm{A}_g.$$

As listed in Table S2 (ESI†), the optical modes E_{1u} and A_{2u} are infrared (IR) active for the $P6_3/mmc$ phase, whereas A_{1g}, E_{1g} and E_{2g} are Raman (R) active. A_{2g}, B_{2g}, B_{1u}, B_{2u} and E_{2u} mode vibrations are nonactive. In the case of *Cmmm* phase, it possesses the point group symmetry of D_{2h}. Only an A_u mode is nonactive with a corresponding frequency of 15.92 meV at the Γ-point. The B_{iu} ($i = 1$, 2, and 3) modes are IR active and can absorb or emit infrared light. At 155.9 GPa, additional information regarding the vibration modes at the Γ point for both the $P6_3/mmc$ and *Cmmm* phases are provided in Table S2 (ESI†). This information will be useful for future Raman and other related experiments.

It is well established that the specific heat C_V and entropy S can be calculated from the total energy and PhDOSs. The temperature dependencies of C_V and S for the $P6_3/mmc$ and *Cmmm* phases of UPt_3 under different pressures are evaluated and exhibited in Fig. 6. In the low-temperature region ($T < 300$ K), pressure significantly affects C_V. For instance, in the $P6_3/mmc$ phase, the C_V values are 195.0 J mol^{-1} K^{-1} and 184.3 J mol^{-1} K^{-1} at 0 GPa and 155.9 GPa, respectively. However, for $T > 300$ K, the C_V values at different pressures approach the Dulong–Petit limit as the temperature increases. Meanwhile, pressure suppresses the increase of S with temperature. Compared to the $P6_3/mmc$ phase, the *Cmmm* phase exhibits lower values of C_V and S, indicating more stable thermodynamic properties at 155.9 GPa. Based on the QHA, the temperature dependence of the bulk modulus $B(T)$, specific heat capacity at constant pressure C_P, and thermal expansion coefficient α_V are calculated at 155.9 GPa, and the *P–T* phase diagram for the $P6_3$/mmc and *Cmmm* is plotted in Fig. 7.

The $B(T)$ of the $P6_3/mmc$ and *Cmmm* decreases by 3.63% and 2.74%, respectively, when the temperature increases to 1000 K [see Fig. 7(a)]. The $B(T)$ of the *Cmmm* phase is less sensitive to temperature compared to the $P6_3/mmc$ phase. At the same time, the C_P and α_V for *Cmmm* are slightly lower than those of the $P6_3/mmc$ in the overall temperature range at 155.9 GPa. The *P–T* phase diagram [Fig. 7(d)] of the two phases of UPt_3 is revealed by comparing the free energies (Fig. S9, ESI†) of the two phases as a function of temperature. Note that the calculated values of the transition pressure are 158 and 160 GPa at $T = 380$ and 850 K, respectively. Different from the α-U,[64] UO_3[25] and U_2Nb,[56] UPt_3 exhibits a relatively well-defined *P–T* phase diagram, showing its strong stability under extreme conditions.

Conclusions

In conclusion, we have systematically investigated the high-pressure behavior of UPt_3 by employing the PSO method and first-principles calculations. We report the discovery of a novel orthorhombic *Cmmm* phase of UPt_3 that emerges above 155.9 GPa. This phase transition is accompanied by a 2.52% reduction in volume and a 36% shortening of the U–U bond length. Compared with the $P6_3/mmc$ phase, the electronic properties of *Cmmm*-UPt_3 reveal an increased $N(E_F)$ and enhanced itinerant properties of the U 5f orbitals. The phonon dispersion and elastic constants confirm the dynamical and mechanical stability of both phases, with the *Cmmm* phase exhibiting superior mechanical properties, including

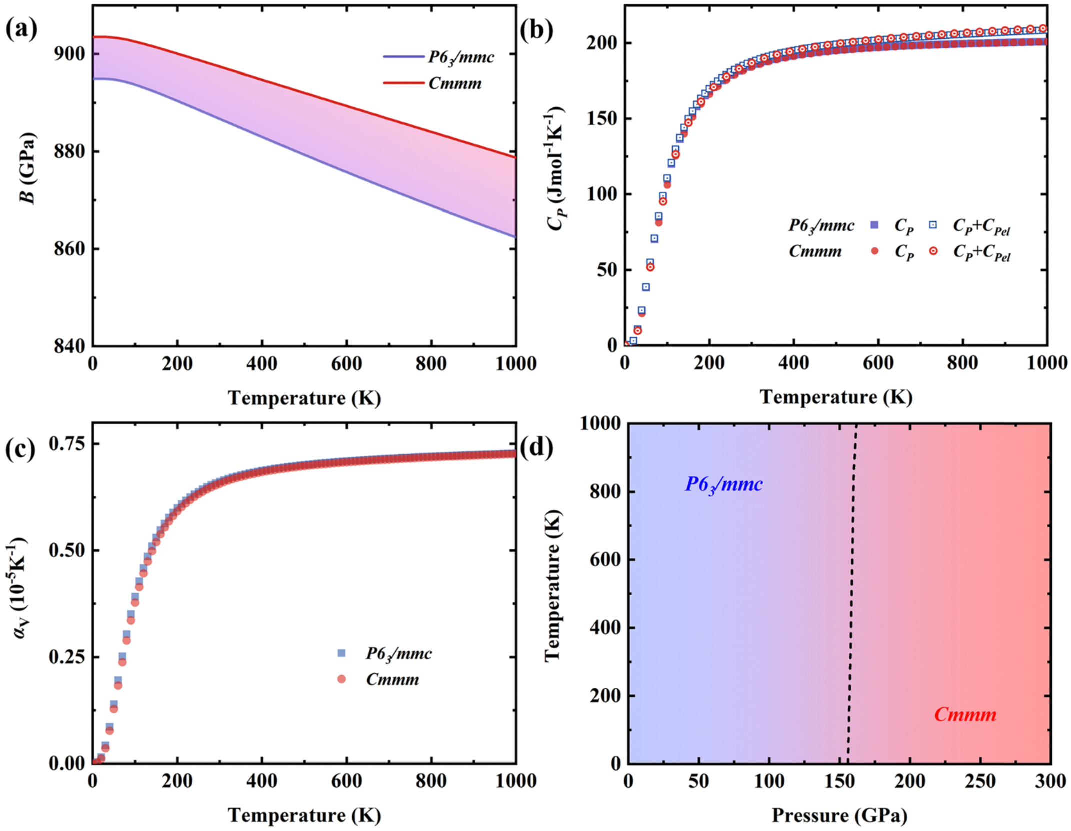

Fig. 7 Temperature dependencies of (a) bulk modulus B, (b) specific heat at constant pressure C_P, and (c) thermal expansion coefficients α_V for UPt_3 at 155.9 GPa. (d) P–T phase diagram of $P6_3/mmc$ and $Cmmm$ phases of UPt_3 computed using the QHA model.

higher bulk modulus, shear modulus, and Young's modulus. With increasing pressure, many mechanical properties are enhanced. Meanwhile, the specific heat, entropy, thermal expansion coefficients, and P–T phase diagram of UPt_3 are calculated and analyzed. Our work provides a theoretical basis for an important uranium-based heavy fermion metal UPt_3 under extreme conditions. The quantum states of chiral superconductivity and topological state in our predicted high-pressure *Cmmm* phase deserve theoretical and experimental efforts in the future.

Data availability

All data included in this study are available upon request by contacting the corresponding author.

Conflicts of interest

There are no conflicts to declare.

Acknowledgements

The authors gratefully acknowledge financial support from the NSAF (Grant No. U2330104), the National Natural Science Foundation of China (Grant No. 12074381 and 12204482) and the Guangdong Basic and Applied Basic Research Foundation (Grant No. 2024A1515010484). The calculations were performed at the CSNS Scientific Computing Platform of the Institute of High Energy Physics of CAS and the GBA Sub-center of the National HEP Science Data Center.

References

1 G. R. Stewart, *Rev. Mod. Phys.*, 1984, **56**, 755–787.
2 X. Y. Ji, Q. Liu, W. Feng, Y. Zhang, Q. Y. Chen, Y. Liu, Q. Q. Hao, J. Wu, Z. W. Xue, X. G. Zhu, Q. Zhang, X. B. Luo, S. Y. Tan and X. C. Lai, *Phys. Rev. B*, 2024, **109**, 075158.
3 G. Chajewski and D. Kaczorowski, *Phys. Rev. Lett.*, 2024, **132**, 076504.
4 L. Huang and H. Y. Lu, *Phys. Rev. B*, 2024, **109**, 205132.
5 D. Aoki, J. P. Brison, J. Flouquet, K. Ishida, G. Knebel, Y. Tokunaga and Y. Yanase, *J. Phys.: Condens. Matter*, 2022, **34**, 243002.
6 A. Schröder, G. Aeppli, R. Coldea, M. Adams, O. Stockert, H. v Löhneysen, E. Bucher, R. Ramazashvili and P. Coleman, *Nature*, 2000, **407**, 351–355.
7 Y. Shimizu, A. Pourret, G. Knebel, A. Palacio-Morales and D. Aoki, *Phys. Rev. B: Condens. Matter Mater. Phys.*, 2015, **92**, 241101.
8 T. Senthil, M. Vojta and S. Sachdev, *Phys. Rev. B: Condens. Matter Mater. Phys.*, 2004, **69**, 035111.

9 R. Ohashi, J. Tei, Y. Tanaka, T. Mizushima and S. Fujimoto, *Phys. Rev. B*, 2024, **110**, 174521.

10 S. Ran, C. Eckberg, Q. P. Ding, Y. Furukawa, T. Metz, S. R. Saha, I. L. Liu, M. Zic, H. Kim, J. Paglione and N. P. Butch, *Science*, 2019, **365**, 684–687.

11 Y. Tsutsumi, K. Machida, T. Ohmi and M.-a Ozaki, *J. Phys. Soc. Jpn.*, 2012, **81**, 074717.

12 Y. Shimizu, D. Braithwaite, D. Aoki, B. Salce and J.-P. Brison, *Phys. Rev. Lett.*, 2019, **122**, 067001.

13 A. J. Arko, C. G. Olson, D. M. Wieliczka, Z. Fisk and J. L. Smith, *Phys. Rev. Lett.*, 1984, **53**, 2050–2053.

14 A. D. Visser, J. J. M. Franse, A. Menovsky and T. T. M. Palstra, *J. Phys. F: Met. Phys.*, 1984, **14**, L191–L196.

15 W. J. G. E. R. Schemm, C. M. Wishne, W. P. Halperin and A. Kapitulnik, *Science*, 2014, **345**, 190.

16 C. Triola and A. M. Black-Schaffer, *Phys. Rev. B*, 2018, **97**, 064505.

17 S. Adenwalla, S. W. Lin, Q. Z. Ran, Z. Zhao, J. B. Ketterson, J. A. Sauls, L. Taillefer, D. G. Hinks, M. Levy and B. K. Sarma, *Phys. Rev. Lett.*, 1990, **65**, 2298–2301.

18 A. Huxley, P. Rodière, D. M. Paul, N. van Dijk, R. Cubitt and J. Flouquet, *Nature*, 2000, **406**, 160–164.

19 G. Aeppli, E. Bucher, C. Broholm, J. K. Kjems, J. Baumann and J. Hufnagl, *Phys. Rev. Lett.*, 1988, **60**, 615–618.

20 R. Joynt and L. Taillefer, *Rev. Mod. Phys.*, 2002, **74**, 235–294.

21 W. J. Gannon, W. P. Halperin, C. Rastovski, M. R. Eskildsen, P. Dai and A. Stunault, *Phys. Rev. B: Condens. Matter Mater. Phys.*, 2012, **86**, 104510.

22 K. S. Youichi Yanase, *Phys. Rev. B*, 2017, **95**, 224514.

23 I. Kawasaki, K. Takeuchi, S.-i Fujimori, Y. Takeda, H. Yamagami, E. Yamamoto and Y. Haga, *Phys. Rev. B*, 2023, **108**, 165127.

24 B. T. Wang, P. Zhang, R. Lizárraga, I. Di Marco and O. Eriksson, *Phys. Rev. B: Condens. Matter Mater. Phys.*, 2013, **88**, 104107.

25 J. J. Ma, C. B. Zhang, R. Z. Qiu, P. Zhang, B. Y. Ao and B. T. Wang, *Phys. Rev. B*, 2021, **104**, 174103.

26 S. S. Saxena, P. Agarwal, K. Ahilan, F. M. Grosche, R. K. W. Haselwimmer, M. J. Steiner, E. Pugh, I. R. Walker, S. R. Julian, P. Monthoux, G. G. Lonzarich, A. Huxley, I. Sheikin, D. Braithwaite and J. Flouquet, *Nature*, 2000, **406**, 587–592.

27 A. Huxley, I. Sheikin, E. Ressouche, N. Kernavanois, D. Braithwaite, R. Calemczuk and J. Flouquet, *Phys. Rev. B: Condens. Matter Mater. Phys.*, 2001, **63**, 144519.

28 Y. Kitaoka, H. Kotegawa, A. Harada, S. Kawasaki, Y. Kawasaki, Y. Haga, E. Yamamoto, Y. Ōnuki, K. M. Itoh, E. E. Haller and H. Harima, *J. Phys.: Condens. Matter*, 2005, **17**, S975.

29 K. Hu, Y. Y. Zhao, Y. X. Geng, J. Q. Yu and Y. Q. Gu, *Phys. Lett. A*, 2022, **451**, 128401.

30 Y. Deng, E. Lee-Wong, C. M. Moir, R. S. Kumar, N. Swedan, C. Park, D. Y. Popov, Y. Xiao, P. Chow, R. E. Baumbach, R. J. Hemley, P. S. Riseborough and M. B. Maple, *Phys. Rev. B*, 2024, **110**, 075140.

31 U. Benedict, S. Dabos, L. Gerward, J. S. Olsen, J. Beuers, J. C. Spirlet and C. Dufour, *J. Magn. Magn. Mater.*, 1987, **63 & 64**, 403–405.

32 M. Sieck, H. v Löhneysen and L. Taillefer, *Physica B*, 1995, **206–207**, 603–605.

33 T. Trappmann, H. v Löhneysen and L. Taillefer, *Phys. Rev. B: Condens. Matter Mater. Phys.*, 1991, **43**, 13714–13716.

34 N. Dijk, A. D. Visser, J. Franse and L. Taillefer, *J. Low Temp. Phys.*, 1993, **93**, 101–116.

35 J. Gouchi, A. Sumiyama, A. Yamaguchi, G. Motoyama, N. Kimura, E. Yamamoto, Y. Haga and Y. Ōnuki, *Phys. Rev. B*, 2016, **93**, 174514.

36 S. M. Hayden, L. Taillefer, C. Vettier and J. Flouquet, *Phys. Rev. B: Condens. Matter Mater. Phys.*, 1992, **46**, 8675–8678.

37 Y. C. Wang, J. Lv, L. Zhu and Y. M. Ma, *Phys. Rev. B: Condens. Matter Mater. Phys.*, 2010, **82**, 094116.

38 Y. C. Wang, J. Lv, L. Zhu and Y. M. Ma, *Comput. Phys. Commun.*, 2012, **183**, 2063–2070.

39 X. L. Pan, H. X. Song, H. Wang, F. C. Wu, Y. C. Gan, X. R. Chen, Y. Chen and H. Y. Geng, *Acta Mater.*, 2024, **263**, 119489.

40 Y. L. Guo, C. Y. Wang, W. J. Qiu, X. Z. Ke, P. Huai, C. Cheng, Z. Y. Zhu and C. F. Chen, *Phys. Rev. B*, 2016, **94**, 134104.

41 X. H. Wang, M. L. Li, F. W. Zheng and P. Zhang, *Phys. Lett. A*, 2018, **382**, 2959–2964.

42 Y. Cao, H. X. Song, X. Z. Yan, H. Wang, Y. F. Wang, F. C. Wu, L. L. Zhang, Q. Wu and H. Y. Geng, *Phys. Chem. Chem. Phys.*, 2024, **26**, 19228–19235.

43 G. Kresse and J. Hafner, *Phys. Rev. B: Condens. Matter Mater. Phys.*, 1993, **47**, 558–561.

44 G. Kresse and J. Furthmüller, *Comput. Mater. Sci.*, 1996, **6**, 15–50.

45 P. E. Blöchl, *Phys. Rev. B: Condens. Matter Mater. Phys.*, 1994, **50**, 17953–17979.

46 W. Kohn and L. J. Sham, *Phys. Rev.*, 1965, **140**, A1133–A1138.

47 H. J. Monkhorst and J. D. Pack, *Phys. Rev. B*, 1976, **13**, 5188–5192.

48 S. L. Dudarev, G. A. Botton, S. Y. Savrasov, C. J. Humphreys and A. P. Sutton, *Phys. Rev. B: Condens. Matter Mater. Phys.*, 1998, **57**, 1505–1509.

49 H. Quan, L. Li, L. T. Shi, J. J. Ma, R.-z Qiu, W. D. Li, S. N. Li and B. T. Wang, *Mater. Today Commun.*, 2024, **38**, 108337.

50 X. Gonze and C. Lee, *Phys. Rev. B: Condens. Matter Mater. Phys.*, 1997, **55**, 10355–10368.

51 A. Togo and I. Tanaka, *Scr. Mater.*, 2015, **108**, 1–5.

52 A. Siegel, K. Parlinski and U. D. Wdowik, *Phys. Rev. B: Condens. Matter Mater. Phys.*, 2006, **74**, 104116.

53 D. A. Walko, J. I. Hong, T. V. Chandrasekhar Rao, Z. Wawrzak, D. N. Seidman, W. P. Halperin and M. J. Bedzyk, *Phys. Rev. B: Condens. Matter Mater. Phys.*, 2001, **63**, 054522.

54 R. W. Hill, *Proc. Phys. Soc., London, Sect. A*, 2002, **65**, 349.

55 H. H. Hill, *Plutonium and other actinides*, Metallurgical Society of AIME, New York, 1970.

56 X. L. Pan, H. Wang, L. L. Zhang, Y. F. Wang, X. R. Chen, H. Y. Geng and Y. Chen, *J. Nucl. Mater.*, 2023, **579**, 154394.

57 Q. G. Sheng and B. R. Cooper, *J. Appl. Phys.*, 1994, **75**, 7035–7040.

58 A. D. Becke and K. E. Edgecombe, *J. Chem. Phys.*, 1990, **92**, 5397–5403.

59 J. F. Nye, *Physical Properties of Crystals: Their Representation by Tensors and Matrices*, Oxford University Press, Great Britain, 1957.

60 G. Grimvall, B. Magyari-Köpe, V. Ozoliņš and K. A. Persson, *Rev. Mod. Phys.*, 2012, **84**, 945–986.

61 Z.-X. Bai, X. Qu, C.-L. Jiang, Z.-T. Liu and Q.-J. Liu, *Phys. Rev. B*, 2024, **109**, 144105.

62 Z. Jiao, Z.-t Liu, X.-h Li, F.-s Liu and Q.-j Liu, *Acta Mater.*, 2025, **285**, 120667.

63 B. T. Wang, P. Zhang, H.-Y. Liu, W. D. Li and P. Zhang, *J. Appl. Phys.*, 2011, 109.

64 H. J. Zhang, S. N. Li, J. J. Zheng, W. D. Li and B. T. Wang, *Chin. Phys. B*, 2017, **26**, 066104.

65 W. A. Dujana, A. Podder, O. Das, M. Solayman, M. T. Nasir, M. A. Rashid, M. Saiduzzaman and M. A. Hadi, *AIP Adv.*, 2021, **11**, 105205.

66 S. R. Prashant Srivastav, Navin Chaurasiya and Pramod K. Yadawa, *J. Pure Appl. Ultrson.*, 2024, **46**, 3–12.

67 S. Xu, X. Fan, C. Gu, W. Zheng and D. J. Singh, *J. Nucl. Mater.*, 2023, **581**, 154448.